

Evaluation and improvement of a dual-channel method for detection and quantification of high-temperature events based on FireBIRD data



Studienarbeit im Studiengang
Geomatics Engineering
an der Universität Stuttgart

Penghua Li

Stuttgart, May 2017

Supervisor: Dr.-Ing. Simon Manuel Plank
Deutsches Zentrum für Luft- und Raumfahrt (DLR)

Examer: Prof. Dr.-Ing. Uwe Sörge
Universität Stuttgart

Abstract

Key words:

Contents

Abstract	iii
1 Introduction	1
1.1 Introduction	1
1.1.1 Impacts of high-temperature events	1
1.1.2 DLR's missions dedicated to high-temperature events monitoring	2
1.2 Outline of the thesis	2
2 Theoretical background of thermal infrared remote sensing	5
2.1 Principles of thermal infrared remote sensing	5
2.1.1 The thermal infrared domain and atmospheric windows	6
2.1.2 The Planck's law and Stefan-Boltzmann law	7
2.2 A dual-channel method for the identification of subresolution high temperature sources	8
3 The MITIP, an atmospheric correction and image processing method	9
3.1 Data preparation and pre-processing	9
3.1.1 Data preparation	9
3.1.2 Data pre-processing	10
3.2 Procedure of the MITIP	10
3.3 Outcomes of the MITIP	13
4 Validation and improvement of the MITIP	15
4.1 Analysis of normal temperature environments	15
4.1.1 Data preparation and processing	15
4.1.2 Results comparison with MODIS SST and calibration	18
4.1.3 transferability test (SST)	18
4.1.4 Results comparison with MODIS LST and calibration	18
4.1.5 transferability test (LST)	18
4.2 Conclusion of the comparisons and calibrations	18
5 Analysis of high-temperature events	19
5.1 High-temperature events	19
5.1.1 Volcanoes	19
5.1.2 Fire events	19
5.2 Comparison with the results of the Zhukov's algorithm	19
5.2.1 Brief description of Zhukov's algorithm	19
5.2.2 From pixel-based to cluster-based analysis	19
5.2.3 Comparison	19

6 Conclusion and outlook	21
6.1 Conclusion	21
6.2 Outlook	21
Bibliography	23

List of Figures

2.1	The thermal infrared wavelength domain (Kuenzer and Dech, 2013).	6
3.1	Emissivity spectra for soils in the ASTER spectral emissivity database. (a) 3 - 5 μm . (b) 8 - 14 μm . (Li et al., 2013).	12
3.2	Emissivity spectra for four types of vegetation in the ASTER spectral emissivity database. (a) 3 - 5 μm . (b) 8 - 14 μm . (Li et al., 2013).	12
3.3	Emissivity spectra for water, ice and snow in the ASTER spectral emissivity database. (a) 3 - 5 μm . (b) 8 - 14 μm . (Li et al., 2013).	12
4.1	a) MODIS SST. b) MITIP temperature product: surface temperature map in MIR band	16
4.2	a) Selected sub-areas distribution over MITIP surface temperature in MIR band. b) Zoomed-in pictures of two sub-areas	16
4.3	Difference map between MODIS SST and MITIP surface temperature in MIR band	17

List of Tables

1.1	Main FireBIRD camera parameters (Altitude 510km) (Frauenberger et al., 2015)	3
-----	--	---

List of Abbreviations

Chapter 1

Introduction

1.1 Introduction

1.1.1 Impacts of high-temperature events

High Temperature Events (HTE), such as fire hazards and volcanic eruptions, occur widely all over the world and exert great impacts on the environment in both space and time domain from global to local scales. These HTEs, without doubt, play crucial roles for the environmental equilibrium (Chuvieco, 2008). HTEs might bring benefits at appropriate time and places, for example by speeding up the procedure of returning nutrients to the soils after vegetation senescence (Zhukov et al., 2005a). However, the potentially hazardous characteristics of HTEs and the serious lack of knowledge about their fundamental roles in Earth system processes in the context of global climate change and population explosion will cause a multitude of problems (Bowman et al., 2009).

Volcanoes represent a serious potential hazard for both the population and environment. Volcanic eruptions usually cause numerous loss of lives and damages to the surrounding environment (Pergola, Marchese, and Tramutoli, 2004). Besides the devastation caused by lava erupted, another significant and obvious effect of volcanic eruptions is the release of a host of gases and volcanic ashes, which might cause climate change and serious air pollution. The 2010 eruptions of Eyjafjallajökull, a volcano in Iceland, although relatively small for volcanic eruptions, ejected a multitude of ashes into the atmosphere and created unprecedented disruptions to European air traffic during 15 - 20 April 2010, costing the aviation industry an estimated \$250 million per day (Gudmundsson et al., 2010). Furthermore, the population exposed to the eruption, had a higher prevalence of respiratory and mental symptoms (Carlsen et al., 2012).

Fire, another kind of high-temperature event, might be one of the most prevalent of all terrestrial disturbance agents for the modification of the Earth's surface and occurs worldwide (Bond and Wilgen, 1996). On one hand, fires in forests stimulate vegetation regeneration, increase plant biodiversity and optimize vegetation structure (Moritz et al., 2014). On the other hand, fires, especially severe fires, can burn up vegetation and organics, resulting in hydrophobic layer on the soil surface or at certain depth of the soil, which makes the soil much more prone to be eroded by wind and rain and might lead to desertification in the end (Gabet,

2003).

Due to the threats mentioned above, high-temperature events monitoring becomes more and more important. Besides, because of the huge areas affected by high-temperature events and its potentially dangerous characteristics, a critical role in the monitoring and investigating of HTE belongs to satellite remote sensing. Higher spatial and spectral resolution data is demanded to better detect and quantify high-temperature events.

1.1.2 DLR's missions dedicated to high-temperature events monitoring

The first DLR's satellite specially designed for HTE monitoring was the Bi-spectral InfraRed Detection (BIRD) satellite. The primary objective of the BIRD satellite was detection and quantitative analysis of high-temperature events like fires and volcanoes. The principal BIRD imaging payload includes the HotSpot Recognition System (HSRS) with one channel in Mid-InfraRed (MIR: 3.4 - 4.2 μm) spectral range and one channel in Thermal-InfraRed (TIR: 8.5 - 9.3 μm) spectral range, the Wide-Angle Optoelectronic Stereo Scanner (WAOSS-B) with a nadir channel in Near-Infrared (NIR: 0.84 - 0.90 μm) spectral range. The ground resolution was 185 meters in the NIR channel and 370 meters in the MIR and TIR channels (Zhukov et al., 2005b).

Due to the success of the BIRD mission, DLR continues making efforts to HTE monitoring with the new Fire Recognition with Bi-spectral InfraRed Detector (Fire-BIRD) mission. It consists of two small satellites Technology Experiment carrier (TET-1), launched in July 2012, and Berlin InfraRed Optical System (BIROS), launched in June 2016. Together, these two small satellites form the FireBIRD mini-constellation (Rücker et al., 2011). Both of them carry a HSRS which is identical to BIRD. In addition, there are an additional 3-line VIS camera. Details about the sensors of TET-1 is shown in Table 1.

Because BIROS is still undergoing an extensive testing program and does not put into use yet, the focus lies on TET-1 imageries in this thesis.

1.2 Outline of the thesis

This thesis consist of six chapters. The remaining chapters are organized as follows.

Chapter 2 gives a brief introduction of thermal infrared remote sensing, including the thermal infrared spectrum, atmospheric windows as well as some basic laws important for the quantitating fire pixels' characteristics. Furthermore, a practical and solid method for detection and characterization of sub-pixel fire and its pixel

TABLE 1.1: Main FireBIRD camera parameters (Altitude 510km)
(Frauenberger et al., 2015)

	3 line-VIS camera	2 infrared cameras
Wavelength	Green: 460 - 560 nm Red: 565 - 725 nm NIR: 790 - 930 nm	MWIR: 3.4 - 4.2 μm LWIR: 8.5 - 9.3 μm
Focal length	90.9 mm	46.39 mm
FOV	19.6°	19°
Aperture (F-Number)	3.8	2.0
Detector	CCD lines	CdHgTe arrays
Pixel size	7 $\mu\text{m} \times 7 \mu\text{m}$	30 $\mu\text{m} \times 30 \mu\text{m}$
No. of pixel	3 \times 5,164	2 \times 512 staggered
Quantization	14 bit	14 bit
Ground resolution	42.4 m	356 m
Sampling size	42.4 m	178 m
Swath width	211 km	178 km
In-flight calibration	No	Black body flap
Data rate	max 44 MBit/s nom 11.2 Mbit/s	0.35 MBit/s
Accuracy	100 m at ground	100 m at ground

fraction is reviewed in section 2.2.

Then, a newly developed method, called MITIP, which is used for atmospheric correction and thermal infrared image processing, is introduced in Chapter 3. The required input data for it and the necessary pre-processings are stated in section 3.1. Its procedures and principles, which are based on the theories and method introduced in Chapter 2, are given in section 3.2. Section 3.3 gives a description of the outputs of the MITIP.

Chapter 4 presents the validation and improvements of the MITIP method. Its outputs are compared with the MODIS temperature products, namely MODIS Sea Surface Temperature (SST) and MODIS Land Surface Temperature (LST). These comparisons are done by means of time-series analyses for the purpose of further improvements of the MITIP method and finding suitable scale factors for the radiometric correction of TET-1 imageries. Finally, the calibration results are presented and the tests of the chosen scale factors for transferability with imageries of other test sites are shown as well.

In Chapter 5, the processing results of TET imageries of different test sites from the MITIP method are demonstrated in section 5.1. The outcomes of the MITIP method and the results of Zhukov's algorithm, which is used to process TET-1 imageries originally, are compared in this chapter. In order to do the comparisons, a procedure is developed to convert the pixel-based results to cluster-based results, which is described in section 5.2. The comparison results are presented in

section 5.3.

Finally, the conclusions and outlooks are given in Chapter 6.

Chapter 2

Theoretical background of thermal infrared remote sensing

This chapter reviews some fundamentals of thermal remote sensing (Section 2.1), as well as a useful approach, which is also used in , to identify and determine target temperature of subpixel resolution (Section 2.2).

2.1 Principles of thermal infrared remote sensing

Thermal remote sensing depends on the fact that any object with a temperature above absolute zero (0 K or -273.15 °C) emits electromagnetic (EM) radiation in the infrared range. For example, the Earth we live has an average temperature around 300 K and its peak emittance is near 10 μm , which falls on thermal infrared domain (Tipler and Mosca, 2007; Tetzlaff, 2004). The spectral composition and intensity of the emitted radiation are determined by its surface temperature, which is also called kinetic temperature T_{kin} , and the emissivity of the object (Milman, 2000). The emissivity ε_λ , ε for short, is a ratio of the radiant flux of an object at a certain temperature to the radiant flux of a blackbody at the same temperature (Equation (4.1)), representing the effectiveness of the object in emitting energy as thermal radiation. The blackbody is an idealized physical object that absorbs and re-emits all incident EM radiation, which means its emissivity is 1 (Prakash, 2000; Kuenzer and Dech, 2013). The emissivity varies as a function of wavelength λ and also depends on the surface properties of the object such as surface roughness or color, but is not temperature-dependent (Flynn, Harris, and Wright, 2001).

$$\varepsilon_\lambda = \frac{L_{gb,\lambda}(T_{kin})}{L_{bb,\lambda}(T_{kin})} \quad (2.1)$$

with:

T_{kin} = kinetic temperature [K]

$L_{gb,\lambda}(T_{kin})$ = radiance of an object with temperature T_{kin} at a certain wavelength [$\text{Wm}^{-2}\text{sr}^{-1}\mu\text{m}^{-1}$]

$L_{bb,\lambda}(T_{kin})$ = radiance of blackbody with temperature T_{kin} at a certain wavelength [$\text{Wm}^{-2}\text{sr}^{-1}\mu\text{m}^{-1}$]

The satellite remote sensing sensors responsive in the thermal infrared domain are capable to record the EM radiations emitted by Earth surface objects (Kuenzer and Dech, 2013). With the recorded radiation the derivation of the radiant temperature T_{rad} is possible. Radiant temperature T_{rad} is the actual temperature obtained from the measurement of the sensor, representing temperature of an equivalent blackbody (Prakash, 2000). Notice that the radiant temperature T_{rad} and the kinematic temperature T_{kin} are two different terms and the conversion between them will be introduced later.

2.1.1 The thermal infrared domain and atmospheric windows

There is no strict definition of the thermal infrared domain. Usually, the thermal infrared wavelength domain spread from around 3 to 14 μm . Within this range, there are two atmospheric windows in the 3 - 5 μm range and in the 8 - 14 μm range (Kuenzer and Dech, 2013).

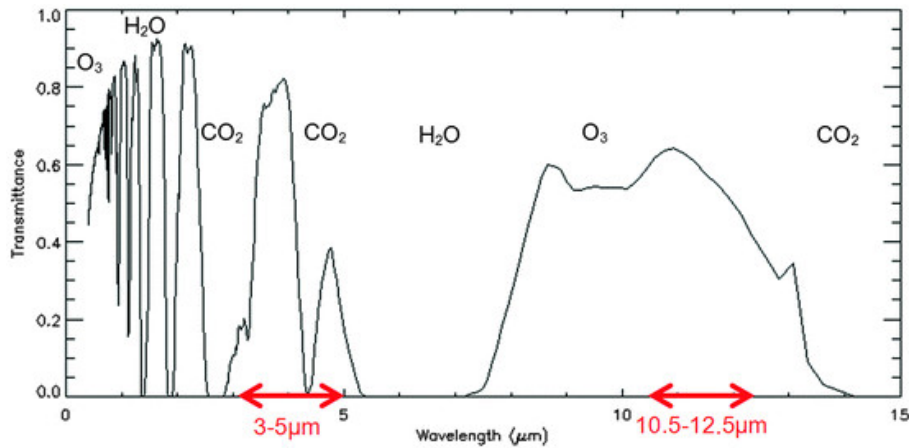


FIGURE 2.1: The thermal infrared wavelength domain (Kuenzer and Dech, 2013).

The spectral range 8 - 14 μm , which is called Long-Wavelength Infrared (LWIR), is the thermal imaging region. Within this range, sensors are able to obtain a completely passive image based on the thermal radiation emitted by objects itself and no illumination is required. There is only a absorption of Ozone in this region which is neglected by sensors. The spectral range 3 - 5 μm is called Mid-Wavelength Infrared (MWIR). Sensors responsive to this spectral range will capture reflected sunlight which contaminates the object-emitted thermal signal. So More attention should be paid when dealing with day-time 3 - 5 μm MWIR imagery.

In this thesis, we focus on the night-time TET-1 scene only.

2.1.2 The Planck's law and Stefan-Boltzmann law

Planck's blackbody radiation law, Planck's law for short, describes the spectral density of electromagnetic radiation $B_\lambda(T_{rad})$ emitted by a blackbody at a given wavelength λ as a function of the blackbody's absolute temperature (Planck, 1900). Given a certain wavelength λ , the spectral radiance $B_\lambda(T_{rad})$ can be computed from the body's temperature:

$$B_\lambda(T_{rad}) = L_{bb,\lambda}(T_{rad}) = \frac{2hc^2}{\lambda^5} \frac{1}{e^{\frac{hc}{\lambda k T_{rad}}} - 1} \quad (2.2)$$

with:

$B_\lambda(T_{rad})$ = spectral radiance of blackbody with temperature T_{rad} at wavelength λ

h = Planck's constant [$6.626 \cdot 10^{34} Js$]

c = speed of light in vacuum [$2.9979246 \cdot 10^8 ms^{-1}$]

λ = wavelength [μm]

e = Euler's number

k = Boltzmann constant [$1.3806 \cdot 10^{-23} JK^{-1}$]

By inverting Equation (2.2), the temperature of a blackbody at a certain wavelength λ can be calculated.

$$T_{rad} = B_\lambda^{-1}(L_{bb}) = \frac{hc}{k \cdot \lambda \cdot \ln\left(\frac{2hc^2}{L_{bb} \cdot \lambda^5 \cdot 10^6} + 1\right)} \quad (2.3)$$

The Stefan-Boltzmann law describes the power radiated from a blackbody in terms of its temperature (Tipler and Mosca, 2007; Walker, Halliday, and Resnick, 2008).

$$T_{Radbb} = \sigma T_{kin}^4 \quad (2.4)$$

with:

T_{Radbb} = Radiant flux of a blackbody [W/m^2]

σ = Stefan-Boltzmann constant [$5.6697 \cdot 10^{-8} W m^{-2} K^{-4}$]

Through Equation (2.4) we can obtain the relationship between the radiant temperature T_{rad} and the kinetic temperature T_{kin} :

$$T_{rad} = \sigma^{\frac{1}{4}} T_{kin} \quad (2.5)$$

For a blackbody whose emissivity $\varepsilon = 1$, its radiant temperature T_{rad} equals kinetic temperature T_{kin} . For all natural materials with an emissivity $\varepsilon < 1$, radiant temperature T_{rad} is always lower than kinetic temperature T_{kin} .

This is a crucial fact in thermal remote sensing data analysis because it reveals how important the emissivity is: objects with the same radiant temperature T_{rad} measured at sensor might vary significantly in their kinetic temperatures T_{kin} due to the considerable differences among their emissivities.

2.2 A dual-channel method for the identification of subresolution high temperature sources

From satellites which contain more than one channel in the thermal infrared spectral region, it is possible to measure surface temperature fields of sub-pixel spatial resolution. Because of the different responses of Planck's function at different wavelength, the radiant temperatures measured in two channels may be expressed in terms of contributions from two temperature fields, each occupying a portion of the pixel (Dozier, 1981; Matson and Dozier, 1981).

As mentioned before, The TET-1 satellite's payload includes a HSRS with two thermal infrared spectral bands, one MIR band and one TIR band. Assume that the TET-1 scene contains sub-pixel high-temperature targets within one "hot pixel". Such a "mixed pixels" composes of a target at temperature T_t , which we call it effective target temperature, occupying portion p , which we call it effective target pixel fraction, of the pixel (where $0 \leq p \leq 1$) and a background temperature T_b which occupies the remaining portion $(1 - p)$. The measured black body radiance $L_{bb,\lambda}$ can be written as:

$$\begin{aligned} L_{bb,1}(T_{rad,1}) &= pL_{bb,1}(T_t) + (1 - p)L_{bb,1}(T_b) \\ L_{bb,2}(T_{rad,2}) &= pL_{bb,2}(T_t) + (1 - p)L_{bb,2}(T_b) \end{aligned} \quad (2.6)$$

where 1 represents the MIR band and 2 represent the TIR band.

If the background temperature T_b is known from neighbor pixels of the hot pixel, these two equations become two linear equations with two unknowns and can be solved easily. For some applications, there is not reliable estimation of the background temperature T_b . Then more complicated method should be applied to solve equations (2.6).

Of course, more than one sub-pixel fire patch might be contained within one hot pixel. Even if only one patch exists, it usually does not have a uniform sub-pixel temperature. This is the reason why we call T_t and p effective, representing an imaginary homogeneous high-temperature event.

Chapter 3

The MITIP, an atmospheric correction and image processing method

This chapter gives a brief description about the MITIP method which is an atmospheric correction and image processing method for the TET-1 imagery, developed by Dr. Rudolf at DLR. Data preparation and pre-processing is given in Section 3.1. The processing procedure is described briefly in Section 3.2. The output of MITIP is presented in Section 3.3.

3.1 Data preparation and pre-processing

3.1.1 Data preparation

The TET-1 imagery inputted to the MITIP is radiometrically calibrated top-of-atmosphere (TOA) radiance data (Level 1B). In order to acquire ground surface radiance and temperature, atmospheric correction should be performed first.

The necessary atmospheric correction takes advantage of the fact that in the thermal spectral range water vapor is the dominating disturbing parameter, while aerosols play only a negligible role (Kuenzer and Dech, 2013). Consequently, for the purpose of simplifying the procedure, water vapor is the only parameter that taken into account while performing atmospheric correction. Because it is impossible to retrieve information of water vapor from TET-1 imagery, external data is required and MODIS water vapor products are used here. Besides, since the water vapor column decreases with elevation, the other parameter that has to be included is the elevation, which is obtained from ASTER Digital Elevation Map (DEM).

From Chapter 2 we know, emissivity map is required to convert the derived radiant temperature T_{rad} to kinetic temperature T_{kin} . The emissivity map can be acquired from ASTER Global Emissivity Database (GED).

Finally, the input files to the MITIP are:

- TET-1 imagery with TOA radiance
- Water vapor from MODIS water vapor product

- Elevation from ASTER Global Elevation Map
- Emissivity map from ASTER Global Emissivity Database

All the auxiliary data can be downloaded from the website of NASA (National Aeronautics and Space Administration).

3.1.2 Data pre-processing

According to the MITIP's requirements, the input data should fulfill three conditions: 1) all input data should be of format GeoTIFF; 2) all input imageries should be overlapped and of the same size; 3) spatial resolution of all imageries should be identical.

On the basis of these requirements, after downloading all the auxiliary data, we should convert them into GeoTIFF format first. Then, compared with TET-1 imagery, the individual raster file of both the ASTER data has a smaller ground coverage of around 60 km by 60 km. These small raster files of ASTER DEM and GED should be merged into one large file respectively which is able to cover the whole area of interest (AOI). Next, to ensure all the four input files are overlapped with each other, they ought to be reprojected into the same and appropriate UTM zone and resampled to the same pixel size. Finally, the TET-1 imagery is used as standard defining the size of the input file. All input data should be clipped using TET-1 imagery as mask to guarantee that they all share the same number of rows and columns.

3.2 Procedure of the MITIP

The radiative transfer function in the thermal region can be expressed as (Kahle, Madura, and Soha, 1980; Kaufman, 1985):

$$L(\lambda) = L_p(\lambda) + \tau(\lambda)\varepsilon(\lambda)L_{bb}(\lambda, T) + \tau(\lambda)(1 - \varepsilon(\lambda))\frac{F(\lambda)}{\pi} + L_{p,s}(\lambda) + \frac{\tau(\lambda)E_g(\lambda)\frac{\rho(\lambda)}{\pi}}{1 - \rho(\lambda)s(\lambda)} \quad (3.1)$$

with:

$L(\lambda)$: at-sensor radiance

$L_p(\lambda)$: thermal path radiance

$\tau(\lambda)$: ground-to-sensor atmospheric transmittance

$\varepsilon(\lambda)$: emissivity

$L_{bb}(\lambda, T)$: blackbody radiance at the ground surface

$F(\lambda)$: thermal downwelling flux on the ground

$L_{p,s}(\lambda)$: solar scattered path radiance

$E_g(\lambda)$: global (direct + diffuse) solar flux on the ground

$s(\lambda)$: spherical albedo
 $\rho(\lambda)$: surface reflectance

As most objects are opaque and do not transmit radiation, we have:

$$\rho(\lambda) = 1 - \varepsilon(\lambda) \quad (3.2)$$

The first line of Equation (3.1) describes the thermal components and the second line the solar radiation. Since in this thesis we restrict ourselves to the night-time TET-1 scenes, the radiative transfer function for the MIR and TIR bands of TET-1 imagery is

$$L(\lambda) = L_p(\lambda) + \tau(\lambda)\varepsilon(\lambda)L_{bb}(\lambda, T) + \tau(\lambda)(1 - \varepsilon(\lambda))\frac{F(\lambda)}{\pi} \quad (3.3)$$

Multiplying both sides of Equation (3.3) with the channel spectral response function $R(\lambda)$ and integrating over the bandpass field we have:

$$L(k) = L_p(k) + \tau(k)\varepsilon(k)L_{bb}(k, T) + \tau(k)(1 - \varepsilon(k))\frac{F(k)}{\pi} \quad (3.4)$$

with:

k = band number; $k = 1$: MIR, $k = 2$: TIR

In most cases of interest to fire detection, the 3 - 5 μm surface emissivity is between 0.75 - 1.0 (Salisbury and D'Aria, 1994), while the 8 - 12 μm emissivity is between 0.95 - 1.0 (W Salisbury and M D'Aria, 1992), as showed in Figure 3.1, 3.2 and 3.3.

Denote the product $\varepsilon(k)L_{bb}(k, T) = L_{surf}^*(k, T)$ as the "effective" or "radiative" surface radiance, we can get:

$$L_{surf}^*(k, T) = \frac{L(k) - L_p(k)}{\tau(k)} - (1 - \varepsilon(k))\frac{F(k)}{\pi} \quad (3.5)$$

Given in both MIR and TIR band the emissivity is close to 1, so the term $1 - \varepsilon(k)$ will be such a small term that the thermal downwelling flux term $F(k)$ will have only a small influence. Finally, all the terms $L_p(k)$, $F(k)$ and $\tau(k)$ will be calculated by MODTRAN (MODerate resolution atmospheric TRANsmission) as a function of atmospheric water vapor column $W(e)$, W for short, which acts as a function of elevation e , for MIR and TIR band of TET-1 imagery respectively.

Finally, the surface radiance of both the black body and natural materials can be calculated from Equation (3.5). The atmospheric correction for the night-time TET-1 scenes are done.

With the help of Planck's function and its inversion, surface temperature for the MIR and TIR band of TET-1 imagery can be derived. Using the dual-channel

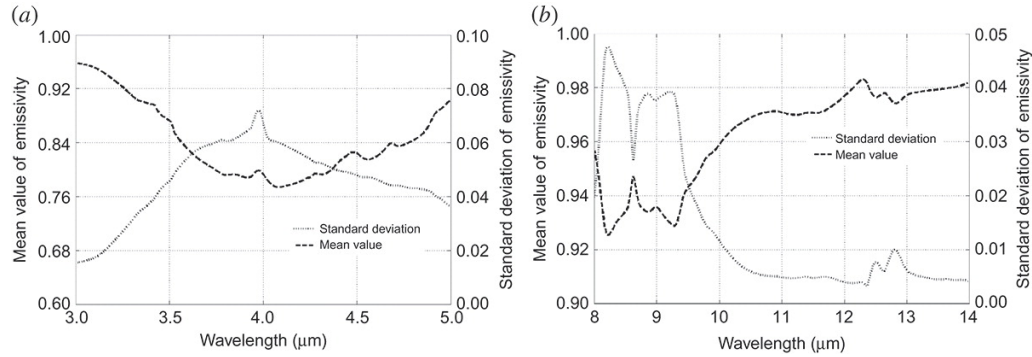


FIGURE 3.1: Emissivity spectra for soils in the ASTER spectral emissivity database. (a) 3 - 5 μm . (b) 8 - 14 μm . (Li et al., 2013).

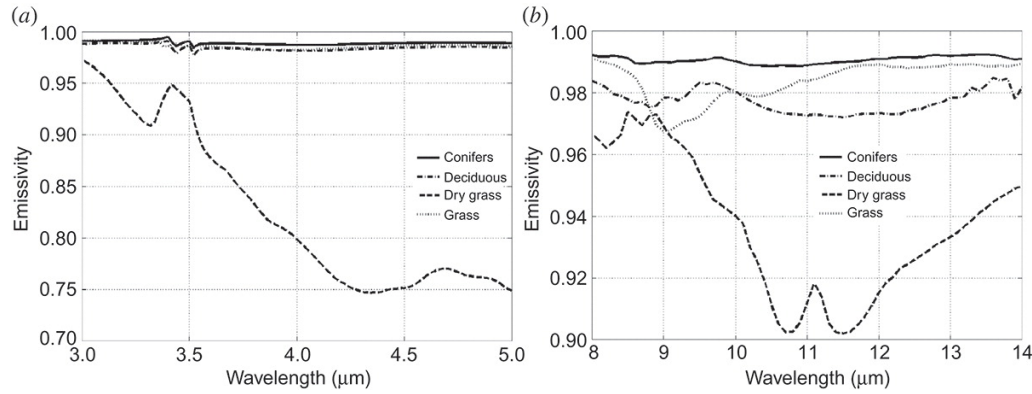


FIGURE 3.2: Emissivity spectra for four types of vegetation in the ASTER spectral emissivity database. (a) 3 - 5 μm . (b) 8 - 14 μm . (Li et al., 2013).

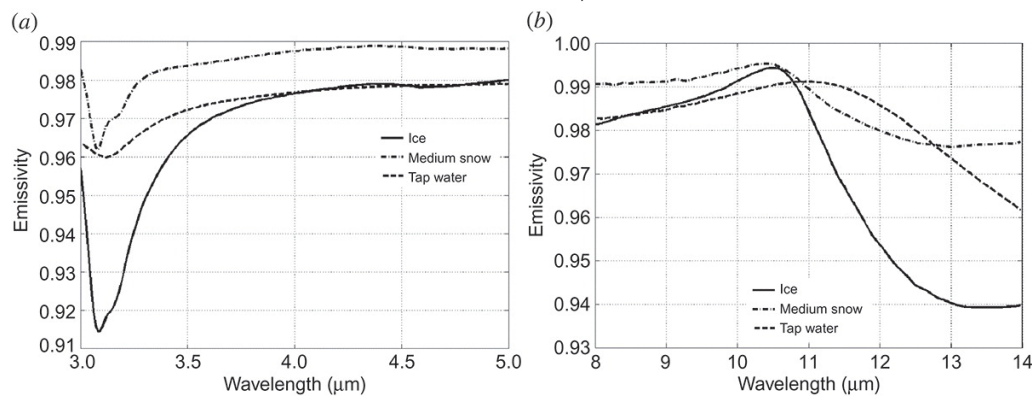


FIGURE 3.3: Emissivity spectra for water, ice and snow in the ASTER spectral emissivity database. (a) 3 - 5 μm . (b) 8 - 14 μm . (Li et al., 2013).

method proposed by Matson and Dozier (1981), the final HTE monitoring products including effective target temperature T_t , effective target pixel fraction and Fire Radiative Power (FRP) can be obtained.

3.3 Outcomes of the MITIP

The outcomes of MITIP can be classified into two parts: one part is the result of atmospheric correction and another the HTE monitoring product.

The result of atmospheric correction is the surface radiance in MIR and TIR band respectively. There are two types of surface radiance files:

- The "blackbody" surface radiance with $\varepsilon_{MIR} = \varepsilon_{TIR} = 1$;
- The "graybody" surface radiance accounting for the input emissivity map ε_{TIR} and assuming $\varepsilon_{MIR} = \varepsilon_{TIR}$;

The HTE monitoring product is one GeoTIFF file which consists of six bands:

- Band 1: surface temperature map in MIR band, T_{MIR} [K];
- Band 2: surface temperature map in TIR band, T_{TIR} [K];
- Band 3: fire probability map indicating which pixel might contain high-temperature events. For non-fire pixels, the pixel value are 0; for each detected fire pixel, the fire probability is assigned between 0.8 to 1.0;
- Band 4: effective target temperature map [K]. For every detected fire pixel, the effective target temperature T_t is calculated. Otherwise the pixel value is set to 0;
- Band 5: effective target pixel fraction map. The same as the effective target temperature map, for each detected fire pixel, the effective target pixel fraction p is calculated. For the rest, their pixel values are set to 0;
- Band 6: fire radiative power (FRP) [MW] map;

If, for one scene, no fire pixels are detected, the output files of HTE monitoring contains only the MIR and TIR band surface temperature maps.

Chapter 4

Validation and improvement of the MITIP

In this chapter, to see whether the temperature products derived from MITIP is reliable or not, its results is compared with MODIS temperature products, namely MODIS Sea Surface Temperature (SST) and MODIS Land Surface Temperature (LST). Two test sites, Etna and Libya, are selected to do the comparisons because their imageries mainly covered by sea (Etna) and homogeneous landscape (Libya) respectively.

4.1 Analysis of normal temperature environments

4.1.1 Data preparation and processing

The MODIS temperature product is downloaded from NASA's website. In order to do the comparison more effectively, the downloaded data will be pre-processed using the same steps described in Chapter 3.

After pre-processing, the MODIS SST product is showed in Figure 4.1. The differences of the surface temperature between MODIS temperature products and MITIP surface temperature maps in MIR and TIR band are computed through the whole imageries respectively. Then, for each scene, several sub-areas which are cloud-free and homogeneous inside are selected as test areas for the comparison. Outliers caused by NoDataValue of MODIS temperature products and cloud e.t.c are filtered out and the mean of the temperature differences ΔT_i inside one sub-area i is calculated.

Finally, the mean value $\overline{\Delta T}$ over all sub-areas within one scene are computed to denote the temperature difference between MODIS temperature products and MITIP results for that scene.

$$\overline{\Delta T} = \frac{\sum_{i=1}^m \Delta T_i}{m} \quad (4.1)$$

with m is the total number of the sub-areas.

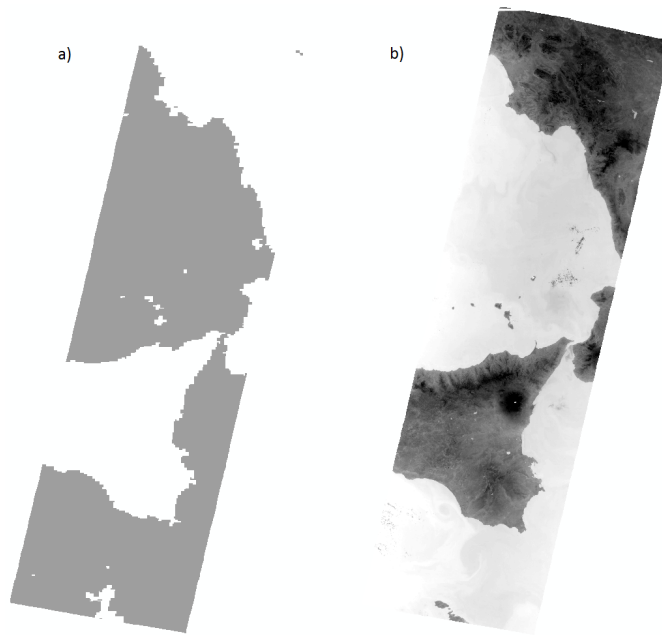


FIGURE 4.1: a) MODIS SST. b) MITIP temperature product: surface temperature map in MIR band

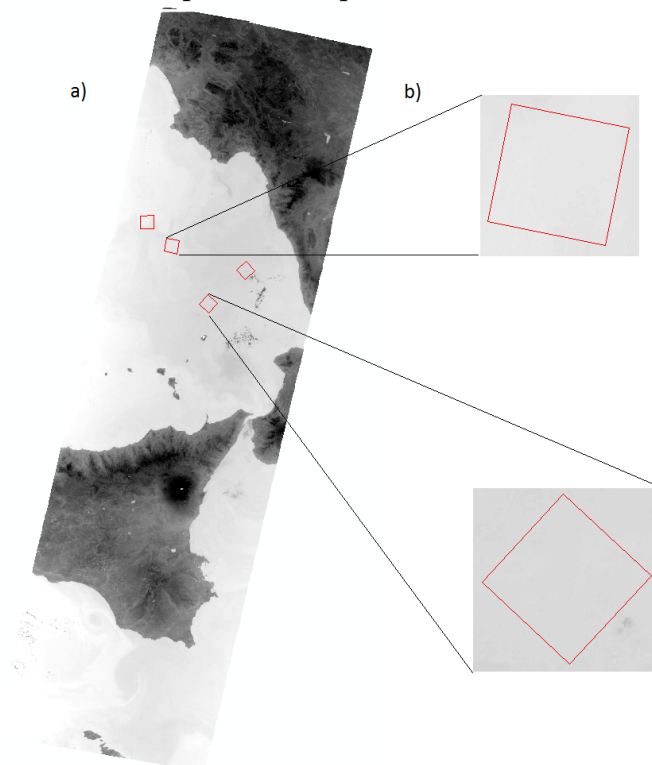


FIGURE 4.2: a) Selected sub-areas distribution over MITIP surface temperature in MIR band. b) Zoomed-in pictures of two sub-areas

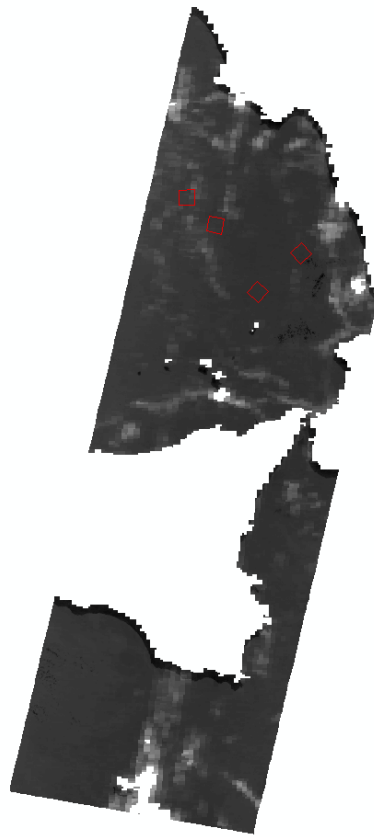


FIGURE 4.3: Difference map between MODIS SST and MITIP surface temperature in MIR band

4.1.2 Results comparison with MODIS SST and calibration

Before doing the comparison between MODIS SST and MITIP surface temperature products, one problem needs to be solved is that the choice of emissivity. The emissivity map derived from ASTER Global Emissivity Database is consisted of 5 bands and there are two bands, namely band 11 with wavelength $8.6\ \mu\text{m}$ and band 12 with wavelength $9.1\ \mu\text{m}$ fall in TET-1 imagery's TIR band with spectral range $8.5\ \mu\text{m}$ to $9.3\ \mu\text{m}$ Reference. So there comes a problem which band of emissivity map should be used.

4.1.3 transferability test (SST)

4.1.4 Results comparison with MODIS LST and calibration

4.1.5 transferability test (LST)

4.2 Conclusion of the comparisons and calibrations

Chapter 5

Analysis of high-temperature events

5.1 High-temperature events

5.1.1 Volcanoes

5.1.2 Fire events

5.2 Comparison with the results of the Zhukov's algorithm

5.2.1 Brief description of Zhukov's algorithm

5.2.2 From pixel-based to cluster-based analysis

5.2.3 Comparision

Chapter 6

Conclusion and outlook

6.1 Conclusion

6.2 Outlook

Bibliography

- Bond, W.J. and B.W. van Wilgen (1996). *Fire and Plants*. Doodrecht, the Netherlands: Springer Netherlands, p. 263.
- Bowman, D.M.J.S. et al. (2009). "Fire in the Earth System". In: *Science* 324, pp. 481–484.
- Carlsen, Hanne Krage et al. (2012). "Health effects following the Eyjafjallajökull volcanic eruption: a cohort study". In: *BMJ Open* 2.6, pp. 1–11.
- Chuvieco, E., ed. (2008). *Earth Observation of Global Change: The Role of Satellite Remote Sensing in Monitoring the Global Environment*. Doodrecht, the Netherlands: Springer Dordrecht, p. 223.
- Dozier, Jeff (1981). "A method for satellite identification of surface temperature fields of subpixel resolution". In: *Remote Sensing of Environment* 11. Supplement C, pp. 221–229.
- Flynn, Luke P., Andrew J.L. Harris, and Robert Wright (2001). "Improved identification of volcanic features using Landsat 7 ETM+". In: *Remote Sensing of Environment* 78.1. Landsat 7, pp. 180–193.
- Frauenberger, Olaf et al. (2015). "Results on verification and validation of OOV-TET1 multi-spectral camera observations within the FireBIRD project". In: *Proc. 10th IAA Symposium Small Satellites for Earth Observation*. Ed. by Rainer Sandau, Hans-Peter Röser, and Arnoldo Valenzuela. Vol. 10. Small Satellites for Earth Observation. Wissenschaft und Technik Verlag Berlin, pp. 163–166.
- Gabet, Emmanuel J. (2003). "Post-fire thin debris flows: sediment transport and numerical modelling". In: *Earth Surface Processes and Landforms* 28.12, pp. 1341–1348.
- Gudmundsson, Magnús T. et al. (2010). "Eruptions of Eyjafjallajökull Volcano, Iceland". In: *Eos, Transactions American Geophysical Union* 91.21, pp. 190–191.
- Kahle, Anne B., Daryl P. Madura, and James M. Soha (1980). "Middle infrared multispectral aircraft scanner data: analysis for geological applications". In: *Applied Optics* 19.14, pp. 2279–2290.
- Kaufman, Yoram J. (1985). "The atmospheric effect on the separability of field classes measured from satellites". In: *Remote Sensing of Environment* 18.1, pp. 21–34.
- Kuenzer, Claudia and Stefan Dech (2013). *Thermal Infrared Remote Sensing: Sensors, Methods, Applications*. Vol. 17. Springer Dordrecht, p. 537.
- Li, Zhao-Liang et al. (2013). "Land surface emissivity retrieval from satellite data". In: *International Journal of Remote Sensing* 34.9-10, pp. 3084–3127.
- Matson, M and Jeff Dozier (1981). "Identification of subresolution high temperature sources using thermal IR sensor". In: *Photogrammetric Engineering and Remote Sensing* 47, pp. 1311–1318.
- Milman, Andrew S. (2000). *Mathematical Principles of Remote Sensing: Making Inferences from Noisy Data*. CRC Press, p. 406.

- Moritz, Max A. et al. (2014). "Learning to coexist with wildfire". In: *Nature* 515.7525, pp. 58–66.
- Pergola, N., F. Marchese, and V. Tramutoli (2004). "Automated detection of thermal features of active volcanoes by means of infrared AVHRR records". In: *Remote Sensing of Environment* 93.3, pp. 311–327.
- Planck, Max (1900). "Entropie und Temperatur strahlender Wärme". In: *Annalen der Physik* 306.4, pp. 719–737.
- Prakash, A (2000). "Thermal remote sensing: concepts, issues and applications". In: *International Archives of Photogrammetry and Remote Sensing*. Vol. 33. Amsterdam, pp. 239–243.
- Rücker, Gernot et al. (2011). "High Resolution Active Fire Monitoring for Global Change Analysis: The Upcoming FireBIRD Satellite Mission". In: *Proc. 5th International Wildland Fire Conference, Sun City, South Africa, 9 - 13 May 2011*.
- Salisbury, John W. and Dana M. D'Aria (1994). "Emissivity of terrestrial materials in the 35 m atmospheric window". In: *Remote Sensing of Environment* 47.3, pp. 345–361.
- Tetzlaff, Anke (2004). "Coal fire quantification using ASTER, ETM and BIRD satellite instrument data". PhD thesis. Ludwig-Maximilians-Universität München.
- Tipler, P.A. and G.P. Mosca (2007). *Physics for scientists and engineers*. 6th edition. W. H. Freeman.
- W Salisbury, John and Dana M D'Aria (1992). "Emissivity of terrestrial materials in the 814 m atmospheric window". In: *Remote Sensing of Environment - REMOTE SENS ENVIRON* 42, pp. 83–106.
- Walker, J., D. Halliday, and R. Resnick (2008). *Fundamentals of physics*. 8th edition. New York: Wiley, p. 891.
- Zhukov, B. et al. (2005a). *Experience of detection and quantitative characterization of fires during the experimental small satellite mission BIRD*. Tech. rep. LIDO-Berichtsjahr=2005, p. 96.
- Zhukov, Boris et al. (2005b). "Detection and analysis of high-temperature events in the BIRD mission". In: *Acta Astronautica* 56.1. 4th IAA International Symposium on Small Satellites for Earth Observation, pp. 65–71.